

## RESEARCH METHODS

# High-sensitivity nanoscale chemical imaging with hard x-ray nano-XANES

A. Pattammattel, R. Tappero, M. Ge, Y. S. Chu, X. Huang, Y. Gao, H. Yan\*

Resolving chemical species at the nanoscale is of paramount importance to many scientific and technological developments across a broad spectrum of disciplines. Hard x-rays with excellent penetration power and high chemical sensitivity are suitable for speciation of heterogeneous (thick) materials. Here, we report nanoscale chemical speciation by combining scanning nanoprobe and fluorescence-yield x-ray absorption near-edge structure (nano-XANES). First, the resolving power of nano-XANES was demonstrated by mapping Fe(0) and Fe(III) states of a reference sample composed of stainless steel and hematite nanoparticles with 50-nm scanning steps. Nano-XANES was then used to study the trace secondary phases in lithium iron phosphate (LFP) particles. We observed individual Fe-phosphide nanoparticles in pristine LFP, whereas partially (de)lithiated particles showed Fe-phosphide nanonetworks. These findings shed light on the contradictory reports on Fe-phosphide morphology in the literature. Nano-XANES bridges the capability gap of spectromicroscopy methods and provides exciting research opportunities across multiple disciplines.

## INTRODUCTION

The rapid growth of nanotechnology with its roots expanded to multidisciplinary fields over the past two decades results in an ever-increasing demand on microscopic characterization tools that are capable of unraveling a holistic view of materials' chemical and physical properties with high spatial resolution. A myriad of microscopy tools at different length scales have been used to study multiple aspects of nanomaterials. Transmission electron microscopy (TEM) enables imaging with atomic resolution, and electron energy-loss spectroscopy (EELS) provides a versatile element-specific technique that simultaneously collects chemical state and morphology data (1). However, the narrow energy range (up to 2500 eV) and the requirement for nanometer-scale sample thickness (due to the poor penetration depth and plural scattering) are fundamental limitations of EELS. In contrast, x-rays have a wide energy range, excellent penetration power, and high chemical sensitivity, therefore permitting samples with thickness of tens of micrometers. X-ray absorption spectrum (XAS) is a widely used technique that investigates the chemical state of the absorbing atom, allowing the measurement of its oxidation state and configuration of the surroundings within a few angstrom distance from the absorber. Originally developed as a bulk technique, conventional XAS lacks spatial resolution needed to probe local phenomena in a chemically heterogeneous matrix. Although micro-XAS characterization tools are available at synchrotron facilities (2), the micrometer resolution is not sufficient to study many complex systems that require the knowledge of chemical state variations at the nanoscale.

In recent years, spectroscopic full-field transmission x-ray microscopy (TXM) has emerged as a new tool for chemical imaging at the nanoscale and demonstrated potentials in multidisciplinary fields (3, 4). It offers both high spatial resolution and chemical-specific information through imaging at energy points across the absorption edge of the element of interest. Presently, x-ray absorption near-edge structure (XANES) spectroscopy with sub-50-nm resolution is routinely achieved with TXM-XANES operating mostly in

the hard x-ray regime (5 to 12 keV) (4–7). There are also efforts to extend it to three-dimensional (3D) chemical mapping for battery studies (8). A drawback of this technique is its relatively low detection sensitivity due to the absorption contrast used. As a bright-field imaging technique (signal is not zero in the absence of the sample), statistical noise and background fluctuations hinder the detection of weak signals. For example, for a 100-nm Fe particle, the theoretical absorption contrast across its K-edge is only about 1.2% (pre- to postedge difference), which is not easy to measure with a sufficient confidence for a quantitative analysis. Consequently, the TXM-XANES is not well suited for imaging the chemical state of an element with the trace-level concentrations or thin materials.

In the soft x-ray regime, spectroscopic imaging was reported through scanning transmission x-ray microscopy (STXM) (9–12). It has high absorption contrast (about 50% for 100-nm Fe nanoparticles across the Fe L-edge) but requires relatively thin (sub-micrometer) samples to allow soft x-rays to penetrate through the medium. STXM may also be conducted under total electron-yield and fluorescence-yield mode to enhance the sensitivity (9). The low penetration length of soft x-rays excludes its application from thick and heterogeneous samples in their natural environment. Using hard x-rays and energy loss spectrum, chemical state mapping at the carbon K-edge was realized by x-ray Raman scattering, alleviating the sample thickness requirement (13). However, crystal analyzers are needed, which complicates the setup.

Hard x-ray spectromicroscopy using an x-ray nanoprobe bridges the capability gap between the aforementioned techniques. The energy range offers metal K-edge studies, and the penetration power of hard x-ray allows considerably thick samples. As a dark-field imaging technique (signal is zero in the absence of the sample), the fluorescence contrast provides much higher detection sensitivity in comparison with TXM-XANES. However, hard x-ray scanning microscopy with resolutions <50 nm is very difficult to realize because of various technical challenges (14, 15). Only in the last few years was the resolution of scanning hard x-ray nanoprobe improved to near 10 nm (16, 17). Combining spectroscopy with imaging makes the task even more daunting owing to the chromaticity of the (diffractive or refractive) nanofocusing optics and the

Copyright © 2020  
The Authors, some  
rights reserved;  
exclusive licensee  
American Association  
for the Advancement  
of Science. No claim to  
original U.S. Government  
Works. Distributed  
under a Creative  
Commons Attribution  
NonCommercial  
License 4.0 (CC BY-NC).

National Synchrotron Light Source II, Brookhaven National Laboratory, Upton, NY, USA.  
\*Corresponding author. Email: hyan@bnl.gov

beam instability issue associated with photon energy change. There has been a report of hard x-ray XAS with a 100-nm beam at a few separated points along a co-implanted ZnO nanowire with a conventional micro-XANES technique (18). There was also a report of chemical mapping from fluorescence images that were collected at few energy points below and above the absorption edge, but the full XANES spectra were not obtained (19). Therefore, quantitative chemical imaging achieved with a hard x-ray nanoprobe and single-pixel XANES fitting at the nanoscale is still an uncharted territory. Here, we report the achievement of fluorescence-yield hard x-ray XANES with nanoscale spatial resolution (hereafter referred to as nano-XANES). The scanning mode also enables absorption- and phase-contrast imaging that are acquired simultaneously for additional morphology information.

To demonstrate the confidence of the technique, we first perform a benchmark experiment using a reference sample composed of physically mixed stainless steel and hematite nanoparticles. Using this reference case with well-understood chemical states, we describe experimental procedures and data analysis methods. A comparison with TXM-XANES is also given. We then apply the technique for speciation of  $\text{Li}_x\text{FePO}_4$  (LFP;  $x = 0$  to 1) battery particles that contain trace secondary Fe-phosphide/Fe-phosphocarbide phase. Our study shows that the high spatial resolution and detection sensitivity of nano-XANES provide unique insights into material properties under complex environments. We give a discussion on current challenges and future perspectives of this technique. In short, hard x-ray nano-XANES demonstrates higher detection sensitivity for chemical state mapping over other techniques, less sample thickness requirement, nanoscale spatial resolution, and multimodal imaging capability for correlative studies. We believe that this work represents a remarkable advancement in the development of nanoscale chemical imaging using hard x-rays (14, 15).

## RESULTS

### Nano-XANES acquisition

The nano-XANES experiment was conducted at the Hard X-ray Nanoprobe Beamline (HXN, 3ID) of the National Synchrotron Light Source II (NSLS-II) at Brookhaven National Laboratory (20). As shown in Fig. 1A, a monochromatic beam was selected by a Si (111) monochromator and then focused on the secondary source aperture (SSA) by a mirror in the horizontal direction and a set of compound refractive lens (CRLs) in the vertical direction. The energy bandwidth of the beam is around 1 eV at Fe K-edge (7.1 keV). The microscope sits about 15 m downstream to SSA, and a Fresnel zone plate (FZP) with 30-nm outmost zone width (Applied Nanotools Inc.) was used to focus the beam to a nanospot. An energy-dispersive detector (Vortex, Hitachi) was placed at 90° with respect to the sample to collect fluorescence signals, and a pixel-array detector (Merlin, Quantum Detectors) was positioned at 0.5 m downstream to record transmitted far-field diffraction patterns. Different from conventional XANES measurement where energy is scanned while the position is fixed on the sample, we conducted 2D grid scans with the nanobeam at different energy points, which produced a series of fluorescence images (Fig. 1B). The simultaneously acquired far-field diffraction patterns were used to generate phase images with a higher spatial resolution via ptychography reconstruction (21) (Fig. 1C). We then aligned the elemental maps with MultiStackReg (ImageJ plugin) (22) and created an image stack (i.e., a 3D image

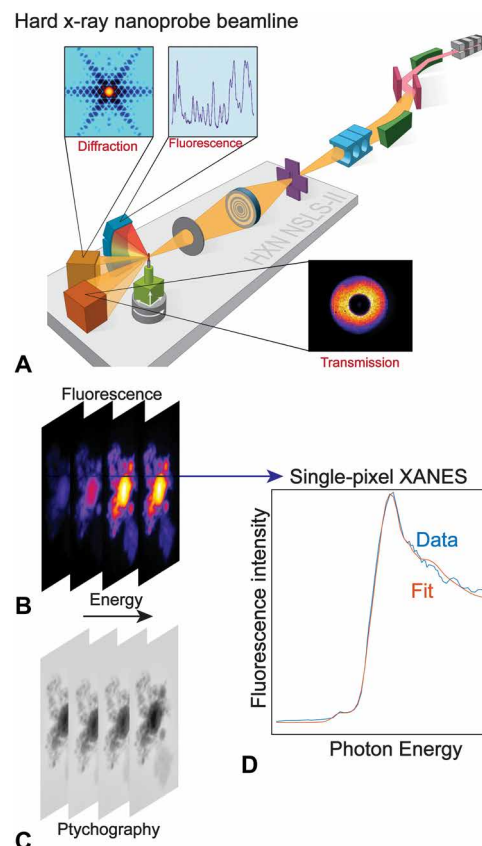


**Fig. 1. Acquisition of nano-XANES.** (A) Schematic of the hard x-ray nanoprobe beamline of NSLS-II. As the sample is raster-scanned by a nanobeam produced from a Fresnel zone plate (FZP), diffraction (not used for samples studied in this work), fluorescence, and transmitted signals can all be collected simultaneously. At energy points along the absorption edge, a series of x-ray fluorescence [nano-x-ray fluorescence (XRF)] maps (B) and phase images from ptychography reconstruction (C) are obtained. (D) Representative fluorescence-yield single-pixel XANES fitted with reference standards.

stack with the third dimension being energy). The Z profile of the image stack at each pixel represents a spectrum at a particular location, which can be fitted with reference spectra to produce spatially resolved chemical state information (Fig. 1D).

Our reference sample contained stainless steel nanoparticles [Fe(0)], hematite nanoparticles [Fe(III)], and their mixture. Their thickness varies from tens to a few hundred nanometers. The Fe(0)/Fe(III) system was chosen for two reasons. First, there are distinguishable spectral features of Fe K-edge XANES, particularly at the pre-edge region (Fig. 2A). Second, accuracy of the fitting methodology can be verified by using Cr-K $\alpha$  fluorescence map as a proxy for Fe(0) (17% Cr in the stainless steel particles). A nano-XANES measurement was conducted across the Fe K-absorption edge (7093 to 7170 eV) with predefined energy points (0.5-eV energy step at the preedge to edge and 1.0 eV at the post-edge). We then used a weighted least-squares fitting algorithm with a nonnegative constraint to calculate the ratio of two Fe species in the mixture.

The biggest technical challenge in nano-XANES acquisition is to maintain the beam stability as the energy varies so that (i) the size and position of the nanobeam do not change, and (ii) the illumination

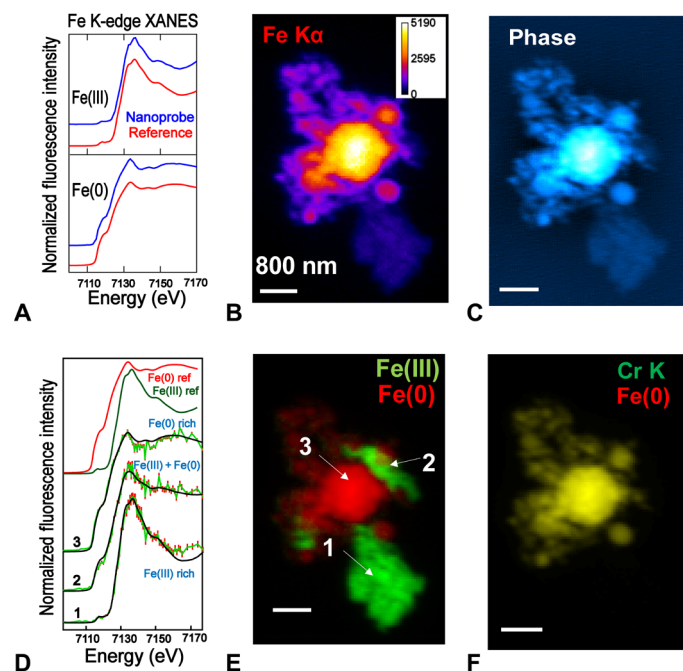


**Fig. 2. Chemical imaging with nano-XANES.** (A) Comparison of summed Fe K-edge nano-XANES spectra of Fe(III) and Fe(0) nanoparticles with the bulk ones. (B) and (C) are Fe-K $\alpha$  XRF and ptychography phase images of hematite [Fe(III)] and stainless steel [Fe(0)] nanoparticle aggregate. (D) Representative single-pixel spectra and their fittings at different locations of the particle are marked in (E), which shows the chemical state map of Fe. (F) XRF map of chromium (alloyed with Fe), overlaid with Fe(0). It confirms the fidelity of the fitting. Scale bars, 800 nm. Data collection details:  $120 \times 80$  points, 50-nm steps, 40-ms dwell time, 77 energy points, and  $\sim 8.2$  hours total acquisition time.

of the lens remains constant. The former ensures that the spatial resolution does not deteriorate, and a postalignment is sufficient to correct any residual position errors. The latter allows an appropriate normalization of the fluorescence intensity. This technical challenge was achieved by aligning the system at predefined energy points and then creating a look-up table to correct motor positions of all components involved in energy change. The long-term stability of the microscope is also critical, since the total acquisition time can take up to 10 hours. The design detail and performance of the microscope can be found elsewhere (20).

To assess the quality of nano-XANES, we first compared the spectrum of each species with a bulk measurement conducted at the X-ray Fluorescence Microprobe Beamline (XFM, 4BM) of NSLS-II, which is a well-established micro-XAS beamline (see the Supplementary Materials for experimental details). Figure 2A clearly shows that the nano-XANES spectral features are identical to those of the reference ones acquired from micro-XANES. A more detailed comparison can be found in fig. S1. It should be noted that the nano-XANES spectra shown in Fig. 2A are the sum of all pixels over a few-micrometer square area for better statistics. Evidently, the summed spectra from different regions are as good as the bulk measurement with the well-resolved pre-edge feature. Our data demonstrate that nanoscale imaging with preedge fitting is possible. This is an important capability for many studies since the 1s-to-3d pre-edge transitions are sensitive to the electronic and geometric structure of the absorbing atom (23).

With the reference spectra available, we can spatially resolve Fe(0) and Fe(III) species in the mixture sample through fitting at individual pixels. Figure 2B shows the Fe-K $\alpha$  fluorescence image at post-edge energy, and Fig. 2C is the corresponding phase image reconstructed from the ptychography reconstruction, which is used mostly for morphology information. Figure 2E depicts the distribution of two species. The dataset has a size of  $120 \times 80 \times 77$ , over a  $4 \times 6 \mu\text{m}^2$  area, and at 77 energy points. The dwell time at each data point was 40 ms, so the total acquisition time was about 8.2 hours. Single-pixel spectrum fitting with reference spectra yields a clear distinction of Fe(0) and Fe(III) regions (Fig. 2D). We see that  $R$  factor, a commonly used metric for XANES fitting models (24), is in the order of  $10^{-3}$ . It confirms the “goodness” of the fit at each pixel level (see fig. S2B). The match between Cr-K $\alpha$  emission (from stainless steel) and deconvoluted Fe(0) and exclusion of Fe(III) regions support the high fidelity of the chemical state mapping (Fig. 2F).

Calculation based on summed pixel intensity from the deconvoluted oxidation maps yields about a 9.2:0.8 ratio of Fe(0) to Fe(III) in the particle. Linear combination fit [using ATHENA program; (24)] of the XANES from the whole particle resulted in a 9.6:0.4 Fe(0)-to-Fe(III) ratio (stainless steel particle,  $96 \pm 1\%$ ; hematite,  $4 \pm 1\%$ ; fig. S2A;  $R$  factor, 0.0015). This low weight percent of Fe(III) phase identified from XANES fitting is considered as questionable in general ( $<5\%$ ), but the nano-XANES images clearly confirm its presence. This result asserts the need for a highly sensitive spatially resolved nano-XANES for trace spectroscopy analysis. Figure 2D displays representative single-pixel XANES randomly selected from identified oxidation state regions marked in Fig. 2E. They clearly show the differences of spectral features at these locations, assuring a reliable single-pixel fitting.

In addition to the fluorescence signal, transmitted diffraction patterns from the nanobeam were recorded on a 2D pixel-array detector simultaneously, allowing absorption- and phase-contrast images to be produced for complementary morphological information. The phase image can be obtained by either differential phase contrast (DPC) imaging (25) or ptychography reconstruction (21). DPC is a deterministic method and measures the phase gradient but lacks the resolution provided by ptychography. Here, we only show the phase image obtained from ptychography (Fig. 2C). One can refer to fig. S3D for a comparison with DPC. Also, to achieve the best result, a maximum likelihood-based ptychography algorithm (26) was used to perform the reconstruction. Generally speaking, fluorescence, absorption, and phase can all be used for XANES measurement. The use of phase, however, is less common because it is relative and cannot be measured directly (27). Unlike the fluorescence imaging, which is a dark-field technique, absorption and phase imaging are both bright-field-based. Therefore, they are more susceptible to noise and background fluctuations, particularly when the signal is weak. In comparison, in fig. S3, we plot XANES spectra obtained from the absorption and phase. Neither of them is good enough to distinguish two states in this case. Nevertheless, they provide complementary morphological information, which the fluorescence alone may not supply.

As we discussed earlier, TXM-XANES is another emerging technique for x-ray spectromicroscopic imaging, but its achievable sensitivity is limited by the absorption contrast. For a comparison, we present TXM-XANES result of the same sample in fig. S3 (A and E), which was measured at the current state-of-the-art Full-field X-ray Imaging Beamline (FXI, 18ID) of NSLS-II (see the Supplementary



Materials for experimental details) (28). Although the absorption edge can be observed by summing spectra over a region of interest, the noise in the data is too big to allow a quantitative analysis. On the basis of these comparisons, we can conclude that fluorescence-yield nano-XANES provides the highest sensitivity for spectromicroscopic imaging.

### Trace secondary phases in lithium iron phosphate particles

The high sensitivity and resolution of nano-XANES provides an excellent imaging tool to study nanoscale chemical changes or evolution at the single-particle level. An immediate utilization of such a technique is to follow the single-particle phase transformations in Li-ion battery materials. We identified olivine-structured lithium iron phosphate ( $\text{LiFePO}_4$ , LFP) as a model system where high chemical contrast and spatial resolution are needed to image chemical changes that dictate the performance of the battery (29). LFP is a prominent cathode material commercially used in Li-ion batteries because of its long cycling life, low cost, and low environmental toxicity (30). Although metal-phosphate batteries are thoroughly studied to enhance the Li storage capacity and cycling efficiency, Li-insertion dynamics is fundamentally intriguing and can be relevant to other electrode materials (11, 31). To enhance the electronic conductivity of LFP particles (LFP), high-temperature carbon coating is routinely used before the electrode preparation. An unexpected side reaction during the high-temperature carbon coating is the formation of nanostructured Fe-rich compounds:  $\text{Fe}_3\text{P}$ ,  $\text{Fe}_2\text{P}$ ,  $\text{FeP}$ , and/or phosphocarbides ( $\text{Fe}_{75}\text{P}_{15}\text{C}_{10}$ ) (29) (for convenience, all these secondary phases are together termed as Fe-phosphides here).

Nanoscale Fe-phosphides in LFP was previously evidenced by x-ray microdiffraction, electron microscopy, and Raman imaging (29, 32). However, the morphology of the secondary phases LFP is under debate, although their formation is in agreement (33). Their differences in chemical composition of LFP (Fe:P, 1:1) and phosphides (Fe:P, 3:1 for  $\text{Fe}_3\text{P}$ ) were used to attain chemical contrast using energy-dispersive x-ray spectroscopy in scanning electron microscopy (SEM). However, the penetration depth was shorter than the particle size so the study was surface sensitive only (32). The Fe K-edge XANES spectra of Fe-phosphate and Fe-phosphide are notably different for phase identification through XANES mapping (Fig. 3). The low abundance of phosphides (<5%) can lead to the suppression of their spectral features in bulk spectroscopy methods. As a result, nano-XANES with high spatial resolution becomes a unique x-ray technique for speciation of heterogeneous matrices such as carbon-coated LFP. It is worth noticing that the XANES spectra of all Fe-phosphides and carbides (because of their similarity in local bonding) are identical. Therefore, spectroscopic differentiation among these phases is not possible with nano-XANES. Here, we use  $\text{Fe}_3\text{P}$  XANES spectrum for chemical mapping along with Fe(II) and Fe(III) references.

Chemical state mapping of carbon-coated LFP showed two spectroscopically distinguishable morphology as LFP particles are cycled. We observed (i) phase-separated Fe-phosphide NPs along with LFP (Fig. 3, A to E) and (ii) Fe-phosphide nanonetworks within the LFP particle (Fig. 3, F to M). Pristine sample exhibited several 100- to 1000-nm particles of Fe-phosphides surrounding the LFP particle (Fig. 3C) with clear grain boundary, in agreement with previous electron microscopy studies (33). XANES spectra from the Fe-phosphides show a good match with  $\text{Fe}_3\text{P}$  reference spectrum, which had a very distinct pre-edge feature (Fig. 3E). XANES spectra

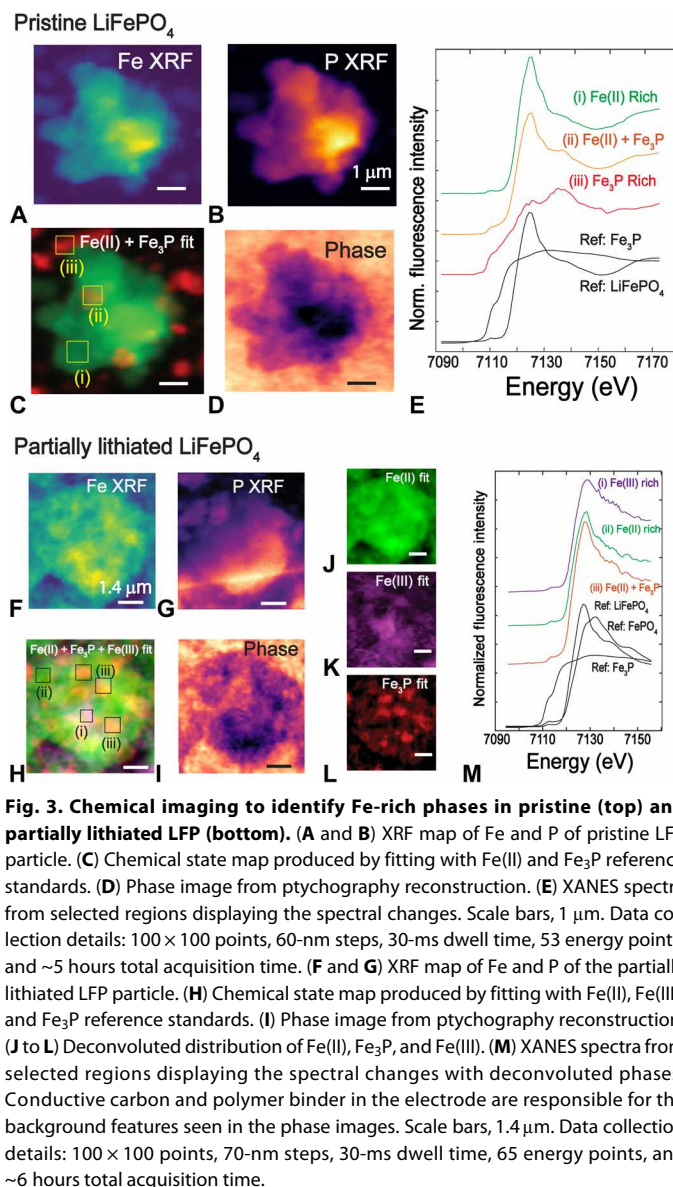


**Fig. 3. Chemical imaging to identify Fe-rich phases in pristine (top) and partially lithiated LFP (bottom).** (A and B) XRF map of Fe and P of pristine LFP particle. (C) Chemical state map produced by fitting with Fe(II) and  $\text{Fe}_3\text{P}$  reference standards. (D) Phase image from Ptychography reconstruction. (E) XANES spectra from selected regions displaying the spectral changes. Scale bars, 1  $\mu\text{m}$ . Data collection details: 100  $\times$  100 points, 60-nm steps, 30-ms dwell time, 53 energy points, and ~5 hours total acquisition time. (F and G) XRF map of Fe and P of the partially lithiated LFP particle. (H) Chemical state map produced by fitting with Fe(II), Fe(III), and  $\text{Fe}_3\text{P}$  reference standards. (I) Phase image from Ptychography reconstruction. (J to L) Deconvoluted distribution of Fe(II),  $\text{Fe}_3\text{P}$ , and Fe(III). (M) XANES spectra from selected regions displaying the spectral changes with deconvoluted phases. Conductive carbon and polymer binder in the electrode are responsible for the background features seen in the phase images. Scale bars, 1.4  $\mu\text{m}$ . Data collection details: 100  $\times$  100 points, 70-nm steps, 30-ms dwell time, 65 energy points, and ~6 hours total acquisition time.

from the mixed regions were also distinguishable by the characteristic pre-edge feature, although the absorption edge features were dominated by Fe(II) due to its large abundance. Additional single-pixel spectra and their difference from deconvoluted regions can be found in fig. S5. This again indicates the advantage of using highly sensitive nano-XANES through fluorescence over TXM-XANES in which case the pre-edge resolution is poor. The percentage of Fe-phosphide phase in the field of view was about 5%, based on the fitted coefficients. After partial (de)lithiation of the particles (electrochemical data are shown in fig. S4), phosphide nanophases (4%) formed a network structure (Fig. 3, H and L) along with Fe(II) and Fe(III) states. The morphology difference of phosphides is confirmed with another partially (de)lithiated particle (fig. S6), which showed about 18% phosphide content. Therefore, there is a notable variation of its concentration from particle to particle. The percolating phosphide nanonetworks were a subject of debate, and it was

probably due to the lack of chemically sensitive characterization tools with adequate spatial resolution (29).

Because x-rays penetrate through the entire thickness of the sample, without a tomographic scan, we cannot tell whether the Fe-phosphide network is formed on the surface or inside the particle, and it is a subject for future study. SEM images of randomly selected partially lithiated LFP particles in the electrode (fig. S4) did not show any surface morphology that resembles the nanonetwork structure. For the pristine sample, we also found particles with almost no phosphide phases (fig. S7). This would rule out the possibility of radiation-induced formation of phosphides. In addition, phase images from ptychography reconstruction at the first and last energy points do not show any morphological changes (fig. S8). Therefore, radiation damage to the particle unlikely occurred. The observed morphology variations of Fe species in LFP suggest the lack of homogeneity in carbon coating, and a possible transformation of phosphide grains from separate particles to nanonetworks during the electrochemical cycling. However, in situ experiments are warranted to track the variation within the same particle to completely understand this process.

An important inference from this study is that the mechanistic studies on single-particle Li-migration must consider or evaluate the role of secondary phases in electrode materials. LFP was one of the most studied battery materials for mechanistic investigations. In particular, there were several hard x-ray TXM (4, 7) and soft x-ray spectromicroscopy work by investigating the local oxidation state of Fe (11, 12, 31). Noticeably, soft x-ray imaging requires 100- to 200-nm thin LFP particles owing to the high absorption cross section, while hard x-ray TXM needs big particles (a few micrometers and above) for sufficient absorption contrast. Hard x-ray nano-XANES through fluorescence does not have such a thickness limitation. Its high chemical sensitivity and high spatial resolution enable the correlation of chemical state variation and morphology transformation with de(lithiation) processes at the nanoscale. Previous spectromicroscopy and nanodiffraction studies interrogated Li-insertion mechanisms to LFP particles. They found mechanical strain, non-uniform carbon coating, or defects as underlying reasons for the non-uniform spatial distribution of lithiated and nonlithiated domains (11). Here, we emphasize that the phosphide evolution from carbon coating could be another important factor that affects the spatial Li (charge) distribution. Notably, the phase-separated domains in LFP particles identified here resemble the previously mapped spatial inhomogeneity in Li diffusion (10, 11). We suggest that the impact of possible secondary phases must be considered while studying Li-ion diffusion kinetics through (similar) cathode particles, for which the presented nano-XANES becomes a unique characterization tool with high penetration depth and detection sensitivity.

## DISCUSSION

Hard x-ray nano-XANES through fluorescence bridges the capability gap of current spectromicroscopy techniques. The use of hard x-rays mitigates the sample preparation challenges in EELS and soft x-ray microscopy, where submicrometer thickness is required. An additional limit on the sample thickness of this technique is the depth of focus, within which the size of the nanobeam is invariant. The sample must be thinner than that to preserve the high spatial resolution provided by the nanobeam. For the nanofocusing optics used in this work, the depth of focus is 21  $\mu\text{m}$ . The dark-field fluorescence

imaging remarkably enhances its detection sensitivity as compared to other bright-field-based techniques such as TXM. The availability of multiple imaging modalities makes it possible for correlative research without additional experimental efforts. We foresee a broad application of hard x-ray nano-XANES for nanospeciation of catalytic systems, electrode materials, environmental pollutants, and bio-nanosystems. However, there are several challenges associated with this technique.

The first challenge is the self-absorption problem for thick and dense samples (also referred to as overabsorption). Absorption occurs along two paths. The incident beam is attenuated in the sample before it hits an emitter and excites fluorescence photons, which will also be attenuated before reaching the energy-dispersive detector. For a quantitative measure of the absolute element concentration, both effects have to be corrected, and the calculation can be complicated. (34) For spectra fitting, if we only care about the chemical state, but not the absolute concentration, only the former matters because what changes markedly across the absorption edge is the absorption coefficient of the incident photon with respect to the element of interest. Self-absorption correction adjusts the intensity of the fluorescence spectra with a priori knowledge on the 3D stoichiometry of the sample (34). For two examples presented in this work, both samples have a thickness much smaller than the absorption length, so no correction was performed. The attenuation length of stainless steel was 3.2  $\mu\text{m}$ , and that of hematite and LFP was 6.4 and 16.8  $\mu\text{m}$ , respectively, at the Fe K-edge. A simple self-absorption correction of the spectra using ATHENA program (24) shows that, for these two cases, this effect is negligible. Nevertheless, self-absorption correction considering the thickness and stoichiometry is required for a much thicker sample.

The second challenge is radiation damage. The flux within the nanobeam is about  $10^9$  photons/s, which is concentrated on a  $\sim 40 \times 40 \text{ nm}^2$  area, thereby leading to an extremely high-flux density. X-ray-induced damage can be a potential problem in nano-XANES experiments because they can last 4 to 8 hours on average. In comparison, in TXM-XANES, the flux is about  $10^{12}$  photons/s over a  $40 \times 40 \mu\text{m}^2$  area, and one measurement takes about 2 min (28). For the same imaged area, the total number of photons delivered to the sample in nano-XANES can be one order of magnitude higher than that in TXM-XANES. A remediation is to increase the solid angle of the fluorescence detector so that more fluorescence photons can be captured.

The third challenge is the slow imaging speed. Each image of nano-XANES is acquired by raster-scanning the sample, unlike the snapshot in TXM-XANES. Mechanical constraints on the scanning stage and signal strength both impose limitations on the imaging speed. Scanning at a few kilohertz rates has been demonstrated for scanning x-ray microscopy (35). Therefore, signal strength is more of a bottleneck here. The slow acquisition speed makes tomographic nano-XANES that would require 400 to 800 hours, which is impractical now.

Looking forward, we can expand the technique along either the spatial or the energy axis. Worldwide efforts of developing the fourth-generation diffraction-limited storage ring will enable a lot higher coherent flux from the source (36). The continuous advancement in high-efficiency optics will focus more photons to the sample (37). Collectively, two orders of magnitude reduction in data collection time is within reach in the near future. In addition, recent efforts of applying machine learning to tomography have made the 3D reconstruction possible with limited projection angles

(38). These advancements can further reduce the collection time. Therefore, there is a strong reason to believe that tomographic nano-XANES through fluorescence is on the horizon. On the data analysis side, current developments on data mining algorithms on spectroscopy data (6) have shown the discovery of hidden or unexpected phases. Applying these analyzing techniques can greatly enhance the detection capability of nano-XANES for trace chemical phases. In an orthogonal direction, expanding the energy range to the region for extended x-ray absorption fine structure (EXAFS) can realize nano-EXAFS imaging for higher chemical specificity and also allow modeling of local bonding structures.

## MATERIALS AND METHODS

Stainless steel and hematite nanoparticles were purchased from U.S. Research Nanomaterials Inc. (Houston, TX). A custom-made 10- $\mu\text{m}$ -thick SiN membrane with 50-nm Pt + Cr fiducial markers was purchased from Norcada Inc. (Part number NCT4155P-III-CrPt). Carbon-coated (1.3% C) lithium iron phosphate powder (<10  $\mu\text{m}$ ), lithium metal anode (600  $\mu\text{m}$  thick), polyvinylidene fluoride (PVDF; PVDF binder), super C45 conducting black carbon, *N*-methyl pyrrolidone (NMP), and LiPF<sub>6</sub> electrolyte (BASF) were purchased from MTI Corp. (Richmond, CA). Iron phosphides (Fe<sub>3</sub>P and Fe<sub>2</sub>P) and iron(III) phosphate were purchased from Sigma-Aldrich (St. Louis, MO).

## Sample preparation

Nanoparticles were dispersed in acetone by sonicating for 10 min and drop-casted to the SiN membrane. Particles on the membrane were imaged using a Hitachi FlexSEM 1000 operated under 15 kV before the x-ray measurements.

## Electrode preparation and battery cycling

A slurry of lithium iron phosphate, black carbon, and PVDF (80:10:10 ratio) were prepared using NMP as a solvent. Lithium-ion battery cathode was prepared by uniformly pasting the LFP slurry onto a 15- $\mu\text{m}$ -thick aluminum sheet using a doctor's blade and dried in a vacuum oven for 12 hours at 100° to 120°C. Preweighed electrodes were used to fabricate CR-2032 coin-type cells using Li metal as the anode in an Ar-filled glove box. Batteries were cycled at a constant current between a voltage window of 3.0 and 4.0 V at a rate of 0.1 C using an eight-channel battery analyzer (BST8-3, MTI Corporation). After the required cycling, the cells were opened inside the glove box. The cathode was washed with dimethyl carbonate (electrolyte solvent, Sigma-Aldrich) and dried before the microscopy studies. Particles on the electrode were imaged using a Hitachi FlexSEM 1000 operated under 15 kV before the x-ray measurements.

## Nano-XANES measurement

A nano-XANES experiment was conducted at the Hard X-ray Nanoprobe Beamline (HXN, 3ID) at the NSLS-II (Brookhaven National Laboratory, Upton, NY, USA) (16, 20). X-rays emitted from the undulator source was first collimated by a mirror, and monochromatized by a double-crystal Si (111) monochromator, with a monochromaticity of about  $1.3 \times 10^{-4}$ . A horizontal focusing mirror and an array of 1D (vertical) beryllium CRLs focus the monochromatic beam to the SSA, where the virtual source is shaped to achieve the desired degree of coherence at the position

of the nanofocusing optics. An FZP was used to focus the incoming beam to a nearly diffraction-limited spot of ~40 nm, and the sample was raster-scanned to produce an image. A beam-stop and order-sorting aperture were used to reject the direct beam and higher-order diffractions. At each energy point (minimum  $\Delta E = 0.5$  eV) for nano-XANES scan, undulator gap, and monochromator, CRLs and FZP positions were adjusted on the basis of the precharacterized look-up table. A Vortex Silicon-drift x-ray fluorescence detector, positioned at 90° to the sample, collected the fluorescence signals. A Merlin detector collected the transmission x-ray patterns simultaneously. The Fe-K $\alpha$  emission was recorded to produce x-ray fluorescence (XRF) images and was normalized with the incoming flux measured by an ion chamber. The fluorescence data analysis was performed with the pyXRF program (39). XRF images at energy points across the absorption edge were stacked and aligned using ImageJ plugin MultiStackReg for alignment (22). DPC and ptychography reconstruction images were produced from transmission data using an in-house program (40).

## SUPPLEMENTARY MATERIALS

Supplementary material for this article is available at <http://advances.sciencemag.org/cgi/content/full/6/37/eabb3615/DC1>

[View/request a protocol for this paper from Bio-protocol.](#)

## REFERENCES AND NOTES

1. R. F. Egerton, *Electron Energy-Loss Spectroscopy in the Electron Microscope* (Springer Science & Business Media, 2011).
2. M. Newville, S. Sutton, M. Rivers, P. Eng, Micro-beam x-ray absorption and fluorescence spectroscopies at GSECARS: APS beamline 13ID. *J. Synchrotron Radiat.* **6**, 353–355 (1999).
3. G. J. Nelson, W. M. Harris, J. R. Izzo Jr., K. N. Grew, W. K. Chiu, Y. S. Chu, J. Yi, J. C. Andrews, Y. Liu, P. Pianetta, Three-dimensional mapping of nickel oxidation states using full field x-ray absorption near edge structure nanotomography. *Appl. Phys. Lett.* **98**, 173109 (2011).
4. J. Wang, Y.-c. K. Chen-Wiegart, J. Wang, In operando tracking phase transformation evolution of lithium iron phosphate with hard x-ray microscopy. *Nat. Commun.* **5**, 1–10 (2014).
5. H. Yang, H. H. Wu, M. Ge, L. Li, Y. Yuan, Q. Yao, J. Chen, L. Xia, J. Zheng, Z. Chen, J. Duan, K. Kisslinger, X. C. Zeng, W.-K. Lee, Q. Zhang, J. Lu, Simultaneously dual modification of Ni-rich layered oxide cathode for high-energy lithium-ion batteries. *Adv. Funct. Mater.* **29**, 1808825 (2019).
6. K. Zhang, F. Ren, X. Wang, E. Hu, Y. Xu, X.-Q. Yang, H. Li, L. Chen, P. Pianetta, A. Mehta, X. Yu, Y. Liu, Finding a needle in the haystack: Identification of functionally important minority phases in an operating battery. *Nano Lett.* **17**, 7782–7788 (2017).
7. U. Boesenberg, F. Meirer, Y. Liu, A. K. Shukla, R. Dell'Anna, T. Tyliczszak, G. Chen, J. C. Andrews, T. J. Richardson, R. Kostecki, J. Cabana, Mesoscale phase distribution in single particles of LiFePO<sub>4</sub> following lithium deintercalation. *Chem. Mater.* **25**, 1664–1672 (2013).
8. Y. Xu, E. Hu, K. Zhang, X. Wang, V. Borzenets, Z. Sun, P. Pianetta, X. Yu, Y. Liu, X.-Q. Yang, H. Li, In situ visualization of state-of-charge heterogeneity within a LiCoO<sub>2</sub> particle that evolves upon cycling at different rates. *ACS Energy Lett.* **2**, 1240–1245 (2017).
9. G. V. Tendeloo, D. V. Dyck, S. J. Pennycook, A. P. Hitchcock, Soft x-ray imaging and spectromicroscopy, in *Handbook of Nanoscopy*, G. V. Tendeloo, D. V. Dyck, S. J. Pennycook, Eds. (Wiley VCH Press, 2012), pp. 745–791.
10. Y. Li, H. Chen, K. Lim, H. D. Deng, J. Lim, D. Fraggedakis, P. M. Attia, S. C. Lee, N. Jin, J. Moškon, Z. Guan, W. E. Gent, J. Hong, Y.-S. Yu, M. Gaberšček, M. S. Islam, M. Z. Bazant, W. C. Chueh, Fluid-enhanced surface diffusion controls intraparticle phase transformations. *Nat. Mater.* **17**, 915–922 (2018).
11. J. Lim, Y. Li, D. H. Alsem, H. So, S. C. Lee, P. Bai, D. A. Cogswell, X. Liu, N. Jin, Y.-s. Yu, N. J. Salmon, D. A. Shapiro, M. Z. Bazant, T. Tyliczszak, W. C. Chueh, Origin and hysteresis of lithium compositional spatiodynamics within battery primary particles. *Science* **353**, 566–571 (2016).
12. D. A. Shapiro, Y.-S. Yu, T. Tyliczszak, J. Cabana, R. Celestre, W. Chao, K. Kaznatcheev, A. D. Kilcoyne, F. Maia, S. Marchesini, Y. S. Meng, T. Warwick, L. L. Yang, H. A. Padmore, Chemical composition mapping with nanometre resolution by soft x-ray microscopy. *Nat. Photonics* **8**, 765–769 (2014).



13. R. Georgiou, P. Gueriau, C. J. Sahle, S. Bernard, A. Mirone, R. Garrouste, U. Bergmann, J.-P. Rueff, L. Bertrand, Carbon speciation in organic fossils using 2D to 3D x-ray Raman multispectral imaging. *Sci. Adv.* **5**, eaaw5019 (2019).
14. G. E. Ice, J. D. Budai, J. W. L. Pang, The race to x-ray microbeam and nanobeam science. *Science* **334**, 1234–1239 (2011).
15. A. Sakdinawat, D. Attwood, Nanoscale x-ray imaging. *Nat. Photonics* **4**, 840–848 (2010).
16. H. Yan, N. Bouet, J. Zhou, X. Huang, E. Nazaretski, W. Xu, A. P. Cocco, W. K. Chiu, K. S. Brinkman, Y. S. Chu, Multimodal hard x-ray imaging with resolution approaching 10 nm for studies in material science. *Nano Futures* **2**, 011001 (2018).
17. J. C. Da Silva, A. Pacureanu, Y. Yang, S. Bohic, C. Morawe, R. Barrett, P. Cloetens, Efficient concentration of high-energy x-rays for diffraction-limited imaging resolution. *Optica* **4**, 492–495 (2017).
18. J. Segura-Ruiz, G. Martinez-Criado, M. Chu, S. Geburt, C. Ronning, Nano-x-ray absorption spectroscopy of single co-implanted ZnO nanowires. *Nano Lett.* **11**, 5322–5326 (2011).
19. F. T. Ling, H. A. Hunter, J. P. Fitts, C. A. Peters, A. S. Acerbo, X. Huang, H. Yan, E. Nazaretski, Y. S. Chu, Nanospectroscopy captures nanoscale compositional zonation in barite solid solutions. *Sci. Rep.* **8**, 13041 (2018).
20. E. Nazaretski, H. Yan, K. Lauer, N. Bouet, X. Huang, W. Xu, J. Zhou, D. Shu, Y. Hwu, Y. Chu, Design and performance of an x-ray scanning microscope at the hard x-ray nanoprobe beamline of NSLS-II. *J. Synchrotron Radiat.* **24**, 1113–1119 (2017).
21. P. Thibault, M. Dierolf, A. Menzel, O. Bunk, C. David, F. Pfeiffer, High-resolution scanning x-ray diffraction microscopy. *Science* **321**, 379–382 (2008).
22. P. Thevenaz, U. E. Rüttimann, M. Unser, A pyramid approach to subpixel registration based on intensity. *IEEE T Image Process.* **7**, 27–41 (1998).
23. T. E. Westre, P. Kennepohl, J. G. DeWitt, B. Hedman, K. O. Hodgson, E. I. Solomon, A multiplet analysis of Fe K-edge 1s→3d pre-edge features of iron complexes. *J. Am. Chem. Soc.* **119**, 6297–6314 (1997).
24. B. Ravel, M. Newville, ATHENA, ARTEMIS, HEPHAESTUS: Data analysis for X-ray absorption spectroscopy using IFEFFIT. *J. Synchrotron Radiat.* **12**, 537–541 (2005).
25. H. Yan, Y. S. Chu, J. Maser, E. Nazaretski, J. Kim, H. C. Kang, J. J. Lombardo, W. K. S. Chiu, Quantitative x-ray phase imaging at the nanoscale by multilayer Laue lenses. *Sci. Rep.* **3**, 1307 (2013).
26. H. Yan, Ptychographic phase retrieval by proximal algorithms. *New J. Phys.* **22**, 023035 (2020).
27. X. Zhu, A. P. Hitchcock, D. A. Bazylinski, P. Denes, J. Joseph, U. Lins, S. Marchesini, H.-W. Shiu, T. Tyliczszak, D. A. Shapiro, Measuring spectroscopy and magnetism of extracted and intracellular magnetosomes using soft x-ray ptychography. *Proc. Natl. Acad. Sci. U.S.A.* **113**, E8219–E8227 (2016).
28. M. Ge, D. S. Coburn, E. Nazaretski, W. Xu, K. Gofron, H. Xu, Z. Yin, W.-K. Lee, One-minute nano-tomography using hard x-ray full-field transmission microscope. *Appl. Phys. Lett.* **113**, 083109 (2018).
29. P. S. Herle, B. Ellis, N. Coombs, L. F. Nazar, Nano-network electronic conduction in iron and nickel olivine phosphates. *Nat. Mater.* **3**, 147–152 (2004).
30. A. K. Padhi, K. S. Nanjundaswamy, J. B. Goodenough, Phospho-olivines as positive-electrode materials for rechargeable lithium batteries. *J. Electrochem. Soc.* **144**, 1188–1194 (1997).
31. Y. Li, F. El Gabaly, T. R. Ferguson, R. B. Smith, N. C. Bartelt, J. D. Sugar, K. R. Fenton, D. A. Cogswell, A. D. Kilcoyne, T. Tyliczszak, M. Z. Bazant, W. C. Chueh, Current-induced transition from particle-by-particle to concurrent intercalation in phase-separating battery electrodes. *Nat. Mater.* **13**, 1149–1156 (2014).
32. Y. Liu, J. Liu, J. Wang, M. N. Banis, B. Xiao, A. Lushington, W. Xiao, R. Li, T.-K. Sham, G. Liang, X. Sun, Formation of size-dependent and conductive phase on lithium iron phosphate during carbon coating. *Nat. Commun.* **9**, 929 (2018).
33. S.-Y. Chung, J.-G. Kim, Y.-M. Kim, Y.-B. Lee, Three-dimensional morphology of iron phosphide phases in a polycrystalline LiFePO<sub>4</sub> matrix. *Adv. Mater.* **23**, 1398–1403 (2011).
34. Y. Liu, F. Meirer, C. M. Krest, S. Webb, B. M. Weckhuysen, Relating structure and composition with accessibility of a single catalyst particle using correlative 3-dimensional micro-spectroscopy. *Nat. Commun.* **7**, 12634 (2016).
35. J. Deng, C. Preissner, J. A. Klug, S. Mashrafi, C. Roehrig, Y. Jiang, Y. Yao, M. Wojcik, M. D. Wyman, D. Vine, K. Yue, S. Chen, T. Mooney, M. Wang, Z. Feng, D. Jin, Z. Cai, B. Lai, S. Vogt, The velociprobe: An ultrafast hard x-ray nanoprobe for high-resolution ptychographic imaging. *Rev. Sci. Instrum.* **90**, 083701 (2019).
36. M. Yabashi, H. Tanaka, The next ten years of x-ray science. *Nat. Photonics* **11**, 12–14 (2017).
37. K. Li, S. Ali, M. Wojcik, V. De Andrade, X. Huang, H. Yan, Y. S. Chu, E. Nazaretski, A. Pattammattel, C. Jacobsen, Tunable hard x-ray nanofocusing with Fresnel zone plates fabricated using deep etching. *Optica* **7**, 410–416 (2020).
38. A. Goy, G. Rughoobur, S. Li, K. Arthur, A. I. Akinwande, G. Barbastathis, High-resolution limited-angle phase tomography of dense layered objects using deep neural networks. *Proc. Natl. Acad. Sci.* **116**, 19848–19856 (2019).
39. L. Li, H. Yan, W. Xu, D. Yu, A. Heroux, W.-K. Lee, S. I. Campbell, Y. S. Chu, in *X-Ray Nanoimaging: Instruments and Methods III* (International Society for Optics and Photonics, 2017), vol. 10389, pp. 103890U.
40. Z. Dong, Y.-L. L. Fang, X. Huang, H. Yan, S. Ha, W. Xu, Y. S. Chu, S. I. Campbell, M. Lin, in *2018 New York Scientific Data Summit (NYSDS)* (IEEE, 2018), pp. 1–5.

#### Acknowledgments

**Funding:** This research used 3ID, 18ID, and 48M beamlines of the National Synchrotron Light Source II, a U.S. Department of Energy (DOE) Office of Science User Facility operated for the DOE Office of Science by Brookhaven National Laboratory under contract no. DE-SC0012704.

**Author contributions:** H.Y. conceived the idea. H.Y. and A.P. designed the experiments. H.Y., A.P., X.H., M.G., R.T., Y.S.C., and Y.G. performed the experiments. H.Y. and A.P. analyzed the data, and all authors contributed to the manuscript. **Competing interests:** The authors declare that they have no competing interests. **Data and materials availability:** All data needed to evaluate the conclusions in the paper are present in the paper and/or the Supplementary Materials. Additional data related to this paper may be requested from the authors.

Submitted 18 February 2020

Accepted 22 July 2020

Published 9 September 2020

10.1126/sciadv.abb3615

**Citation:** A. Pattammattel, R. Tapper, M. Ge, Y. S. Chu, X. Huang, Y. Gao, H. Yan, High-sensitivity nanoscale chemical imaging with hard x-ray nano-XANES. *Sci. Adv.* **6**, eabb3615 (2020).

## High-sensitivity nanoscale chemical imaging with hard x-ray nano-XANES

A. Pattammattel, R. Tappero, M. Ge, Y. S. Chu, X. Huang, Y. Gao, and H. Yan

*Sci. Adv.*, **6** (37), eabb3615.  
DOI: 10.1126/sciadv.abb3615

### View the article online

<https://www.science.org/doi/10.1126/sciadv.abb3615>

### Permissions

<https://www.science.org/help/reprints-and-permissions>

Use of this article is subject to the [Terms of service](#)